Appl. Phys. A 87, 193–198 (2007)
DOI: 10.1007/s00339-006-3818-3

Applied Physics A
Materials Science & Processing

M.F. WU[1,✉]
F.Y. MENG[1]
Q. WU[1]
J. WU[2]
J.C. LEE[3]

An approach for small omnidirectional microstrip antennas based on the backward waves of double negative metamaterials

[1] School of Electronics and Information Technology,
Harbin Institute of Technology, Harbin, Heilongjiang 150001, P.R. China
[2] China Research Institute of Radiowave Propagation, Xinxiang, Henan 453000, P.R. China
[3] School of Electronic Engineering, Kwangwoon University, Seoul 139-137, Korea

Received: 21 August 2006/Accepted: 21 November 2006
Published online: 9 February 2007 • © Springer-Verlag 2007

ABSTRACT In this paper, a small omnidirectional microstrip antenna (MSA) is proposed based on a compact double negative (DNG) metamaterial, which is constructed by modified split ring resonators (MSRRs) and metal strips. First, the backward wave property of the DNG slab is investigated and illustrated by full-wave simulations. It is shown that the slab can exhibit double negative parameters and support backward wave in a broadband of 8.45 GHz ∼ 11.05 GHz, so the existence of the DNG band is proven. Then the DNG unit cells are stacked and embedded into a host substrate to construct a phase-compensating substrate for the small MSA. By using the modified transmission line model (MTLM) and 3D full-wave simulation, a small MSA is modeled and characterized. Results show that the presence of the DNG fillings can indeed greatly reduce the physical dimensions from 0.5λ to 0.17λ, while its farfield pattern is significantly different from that of a conventional half-wavelength MSA. Lastly, the *E*-field distributions of the small MSA and a conventional half-wave-length MSA are contrasted and discussed to explain the functional mechanism of the small omnidirectional SMA.

PACS 78.70.Gq; 81.05.Zx; 84.40.Ba

1 Introduction

Double negative (DNG) metamaterial, represents a new kind of artificially engineered electromagnetic materials by properly inserting periodic inclusions with dimensions smaller than the guided wavelength into a host material. Because DNG can exhibit negative refractive index characteristics resulted from simultaneous negative permittivity and permeability, it has been also referred to as several other names, such as negative refraction index medium (NRI), left-handed material (LHM), and backward wave material (BWM). The basic concept of DNG was introduced by V.G. Veselago in 1968 [1], who concluded that a theoretical medium with simultaneous negative permittivity and permeability could support unusual phenomena when electromagnetic wave passed though it. Experimentally, the first effective DNG was synthesized by Smith et al. in microwave regime [2]. Since then, considerable attention has been arisen, and remarkable progress has been achieved [4–8], which leads to the development of potential applications in mobile communications, medical imaging, and optoelectronics [9–16].

Fundamentally, Enghata has shown that a pair of double positive medium (DPS) and DNG blocks could be used to build small resonators [16], and it has been verified by recent experiments [17]. Here, the hybrid materials could be utilized to support forward and backward waves; thus, the phase shift gained by waves propagating in the DPS block could be compensated by waves in the DNG block. Another important application of the DPS–DNG phase compensator is the miniaturization of microstrip antennas (MSAs). By theoretical analysis, several groups have found that the MSAs' sizes can be reduced by multi-pair dielectric blocks and the dimensions of MSAs would no longer be proportional to the working wavelength but approximately to the ratio of the dimensions of the dielectric blocks [18–21].

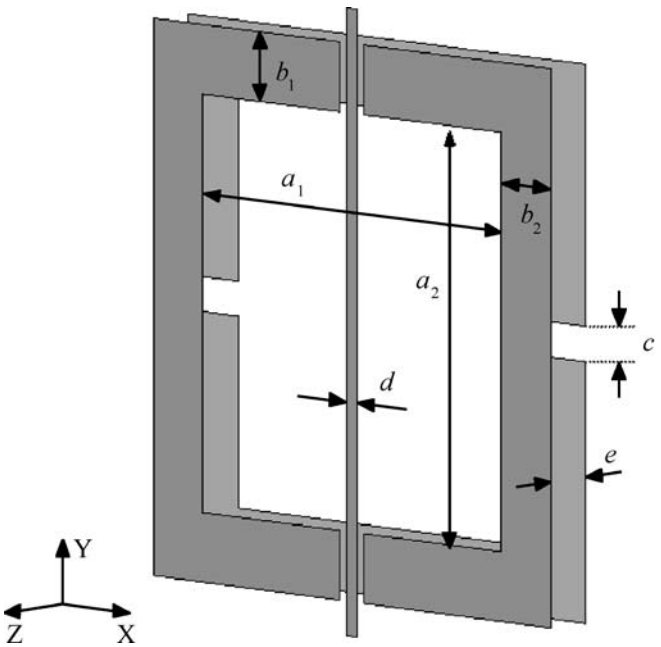

FIGURE 1 Illustration of the configurations of the DNG unit cell

✉ Fax: 86-451-86413502, E-mail: wumingfeng2005@yahoo.com.cn

Although the theoretical results could be promising for the miniaturization of MSAs, further works are greatly necessary, considering the inherent severe dispersion of the practical DNG structures, which is different from that set in the theoretical models. Furthermore, the functional mechanism of the miniaturized MSA should be characterized more clearly and directly to determine that the miniaturization is indeed realized by the backward wave property. Additionally, the unique merits of the MSA with DNG fillings can be evaluated for further experimental investigations based on the contrast of performances between the miniaturized MSA and conventional ones.

2 DNG unit cell and the backward wave property

The configuration of the DNG unit cell is shown in Fig. 1 [22]. It consists of two modified split ring resonators (MSRRs) and one strip embedded in the dielectric host medium with $\varepsilon_r = 2.2$. The MSRR includes two square rings parallel to each other, and each ring has two gaps at opposite sides. The two rings have the same physical sizes, and the back ring (in light gray color) is obtained by rotating the front ring (in dark gray color) 90°. The strip and the front ring (in dark gray color) of the MSRR are on one plane. The related dimensions in Fig. 1 are: $a_1 = a_2 = 1.78$ mm, $b_1 = b_2 = 0.254$ mm, $c = e = 0.17$ mm and $d = 0.048$ mm. The length of the strip is 2.286 mm. The sizes of the unit cell are 2.286 mm × 2.286 mm × 0.51 mm. The metal used here is copper, and the thickness is 0.018 mm.

To prove the presence of the DNG frequency band, the backward wave characteristics will be demonstrated by the MSRRs and strips slab shown in Fig. 2. The simulation configuration consists of a two-port waveguide, formed by a pair of both perfect electric conductor (PEC) and perfect magnetic conductor (PMC) walls, shown as Fig. 2a. Six DNG units are centered in the left waveguide (only four units are depicted for convenience), and the incident wave is guided from left to right side with magnetic field in the z-direction (perpendicular to the MSRR plane) and electric field in the y-direction (along the wire). The right part of the waveguide

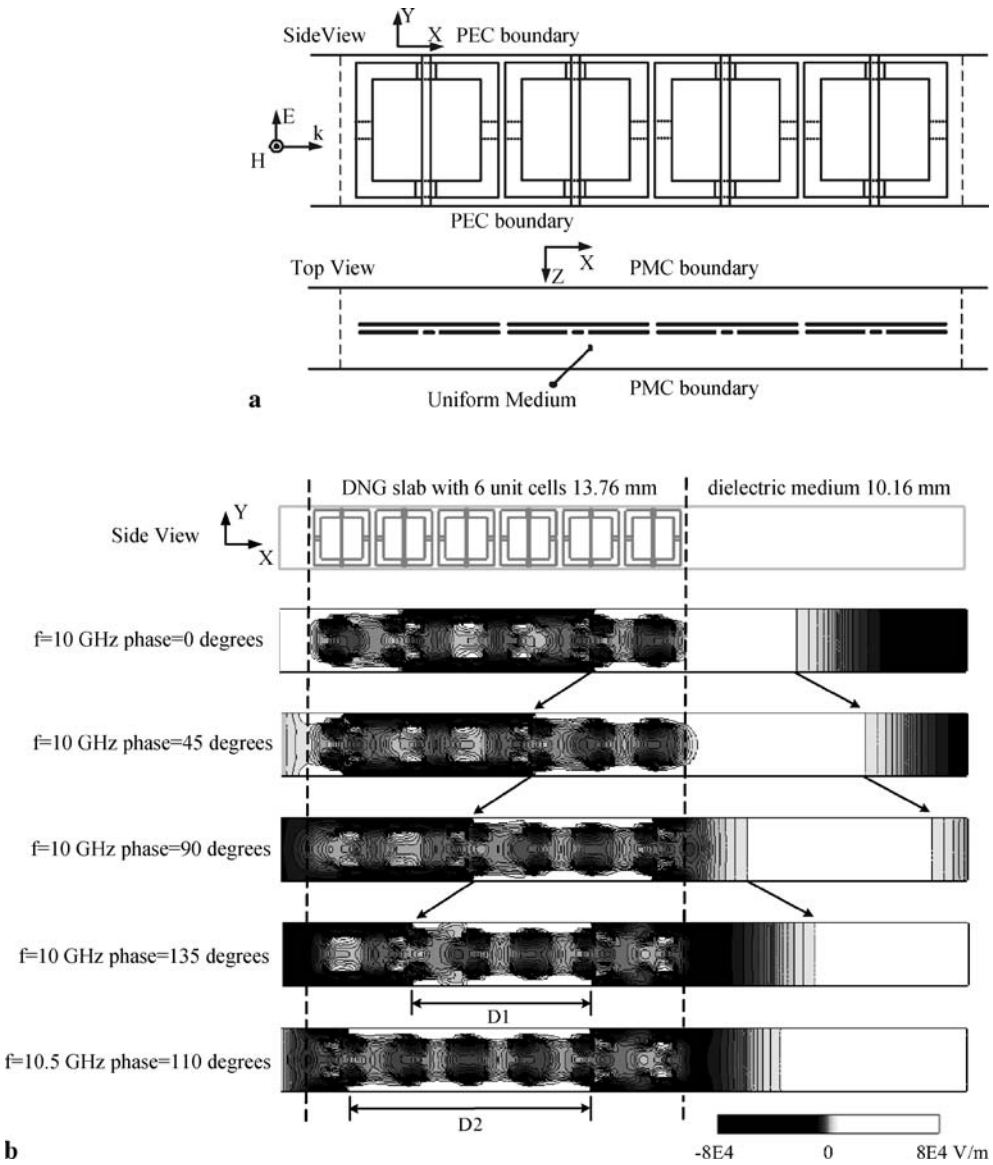

FIGURE 2 Illustration of the backward wave property supported by the DNG slab (**a**) the simulation configuration of the DNG slab (**b**) the backward waves in the DNG slab

is the same dielectric medium as the host medium of the DNG, depicted in Fig. 2b. When the incident wave propagates from the left DNG slab to right normal dielectric medium along $+x$-direction, we obtain the distribution of electric field in the waveguide at 8.45 GHz $\sim$ 11.05 GHz. The simulated E-field magnitude of the 6-cell DNG slab at 10 GHz is illustrated by the snapshots of the contour representation in Fig. 2b.

The phase of the excitation source at 10.0 GHz is stepped through 0, 45, 90, and 135°. The wave front propagates along $+x$-direction in the right normal dielectric medium of the waveguide, but the wave front in the left DNG slab propagates toward the source, which verifies that the wave appears to move in the opposite direction as energy flow in DNG slab. Additionally, the contour of the E-field magnitude at 10.5 GHz is also depicted in Fig. 2b for comparison. It is quite evident that the distance between the neighboring nulls of the half-wavelength E-field becomes larger when the frequency is increased ($D_1 < D_2$). With the field distributions in the DNG, it is found that the phase and group velocities are antiparallel, and the wavelength is proportional to the operating frequency.

3 Modeling and design of the miniaturized microstrip antennas (MSAs)

There is a dilemma, widely concerned, with the traditional design methodology of the MSAs. For conventional materials, to choose a lower dielectric constant substrate may result in a bulky patch with a broader bandwidth; while to choose a higher dielectric constant substrate will reduce the dimensions of the patch, but narrow the bandwidth. After the verification of the backward waves, a novel stage is arisen to break the fundamental dilemma, because it can be promising to reduce the physical dimensions of the patch by the unusual performance of the DNG fillings, as a phase compensator [23]. Due to the mechanism, in this study, we will first construct a composite substrate by combining the DPS and DNG fillings. Nevertheless, when the DNG fillings, embedded into the substrate, are closed to the two radiative ends of the patch, the radiation conductance will be greatly influenced. To reduce the interference, the DNG fillings will be put at the center of patch, leaving the two ends free. Since the DNG fillings are centered and the other two ends are host medium, we name this composite substrate as "DPS-DNG-DPS" substrate. Under the situation, influence of the DNG fillings on the radiation conductance can be neglected, and the patch can be modeled by the modified transmission line model (MTLM).

The discussed MSA, loaded by the DPS-DNG-DPS substrate, is illustrated in Fig. 3. The dimensions of the patch are W_1 in x-direction and W_2 in z-direction. The length of the microstrip feedline is L_f and the width is W_f. The dimensions of the substrate are $(D_1 + W_1 + D_f)$ in x-direction and $(2D_2 + W_2)$ in z-direction, and the high of the substrate is H. For the embedded DNG fillings, 5 unit cells are used along the z-direction and 1 unit cell is used along the x-direction. The 5×1 DNG cells are just put under the patch to leave the two equal ends of the patch free, so we can treat the two ends the same as traditional MSAs. L_R represents the length of the patch loaded by DPS in each end, while L_L represents the length of patch loaded by DNG fillings, and they sum to be the patch length L. The DPS is normal dielectric material with a relative permittivity of 2.2, which is the same as the host dielectric material of the DNG fillings.

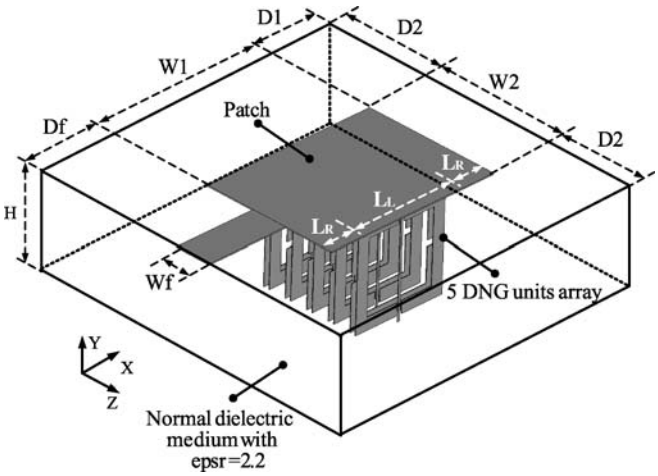

FIGURE 3 Illustration of the geometric configuration of the small microstrip antenna (MSA) loaded by the DPS-DNG-DPS substrate

To derive the analytical expressions of the MSA loaded by DPS-DNG-DPS substrate, the MTLM employed here is shown in Fig. 4. In the MTLM, the G denotes the radiation admittance of the microstrip edges, and C means the edge capacitance to model the microstrip end-effect extension. Y_R and Y_L, respectively, represent the characteristic admittance of the equivalent right-handed transmission line and left-handed transmission line loaded by the DPS and DNG fillings, respectively. Consequently, the input admittance Y_{in} can be stated as following expressions by transmission line theory [24]:

$$Y_{in} = Y_r + Y_R \frac{Y_{in0} + jY_R \tan \beta_R L_R}{Y_R + jY_{in0} \tan \beta_R L_R}, \tag{1}$$

$$Y_{in0} = Y_L \frac{Y_{in1} + jY_L \tan \beta_L L_L}{Y_L + jY_{in1} \tan \beta_L L_L}, \tag{2}$$

$$Y_{in1} = Y_R \frac{Y_r + jY_R \tan \beta_R L_R}{Y_R + jY_r \tan \beta_R L_R}, \tag{3}$$

$$Y_r = G + j\omega C, \tag{4}$$

where

$$Y_R = \frac{W}{h} \frac{\sqrt{\varepsilon_{DPS}}}{\sqrt{\mu_{DPS}}}, \tag{5}$$

$$Y_L = \frac{W}{h} \frac{\sqrt{\varepsilon_{DNG}}}{\sqrt{\mu_{DNG}}}, \tag{6}$$

$$\beta_R = \omega \sqrt{\varepsilon_{DPS}} \sqrt{\mu_{DPS}}, \tag{7}$$

$$\beta_L = \omega \sqrt{\varepsilon_{DNG}} \sqrt{\mu_{DNG}}, \tag{8}$$

$$G = \frac{1}{90} \frac{W_2}{\lambda}, \tag{9}$$

$$C = \frac{2\pi \Delta L Y_R}{\lambda \omega}, \tag{10}$$

$$\Delta L = 0.5H. \tag{11}$$

In the MTLM, the ε_{DNG} and μ_{DNG} are effective parameters used to characterize the macroscopical effects of the DNG

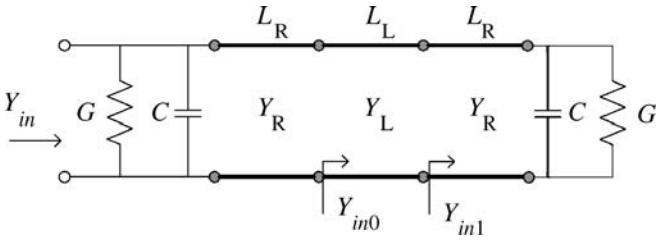

FIGURE 4 Illustration of the modified transmission line model (MTLM) for the small microstrip antenna

unit cell based on effective medium theory. To obtain them, the CST MWS is firstly used to calculate the scattering parameters of the DNG unit cell. Then we can extract the effective permittivity $\varepsilon_{\mathrm{DNG}}$ and permeability μ_{DNG} from scattering parameters by the approach presented in [25]. The variations of the effective permittivity $\varepsilon_{\mathrm{DNG}}$ and permeability μ_{DNG} are demonstrated in Fig. 5. In Fig. 5, the solid gray line marked with circles illustrates the real part of the effective $\varepsilon_{\mathrm{DNG}}$, the solid black line illustrates the imaginary part of the effective $\varepsilon_{\mathrm{DNG}}$, the solid gray line marked with squares illustrates the real part of the effective μ_{DNG}, and the solid black dash line illustrates the imaginary part of the effective μ_{DNG}. It shows that the negative rang of $\varepsilon_{\mathrm{DNG}}$ is at $7.50 \sim 11.05$ GHz, and the negative bands of μ_{DNG} is located at $8.45 \sim 11.75$ GHz. Hence, the unit cell can exhibit DNG properties over $8.45 \sim 11.05$ GHz according to the retrieve approach.

Because the DNG band is located at $8.45 \sim 11.05$ GHz, we choose the 9 GHz as the working frequency. The geometry parameters are as follows: $D_1 = 1.52$ mm, $D_2 = 1.34$ mm, $W_1 = 3.81$ mm, $W_2 = 2.92$ mm, $H = 2.29$ mm, $L_{\mathrm{f}} = 0.76$ mm, $D_{\mathrm{f}} = 1.78$ mm, $L_{\mathrm{R}} = 0.89$ mm, $L_{\mathrm{L}} = 2.03$ mm. The geometric length of the patch is 3.81 mm, about 0.17λ. Here, λ represents the working wavelength of 9 GHz in the host medium with $\varepsilon_{\mathrm{r}} = 2.2$), which is evidently smaller than the 0.5λ limitation.

Calculating the input admittance and the reflection coefficient for the MSA with DNG fillings, we can observe the effects of the phase compensation on the antenna dimensions

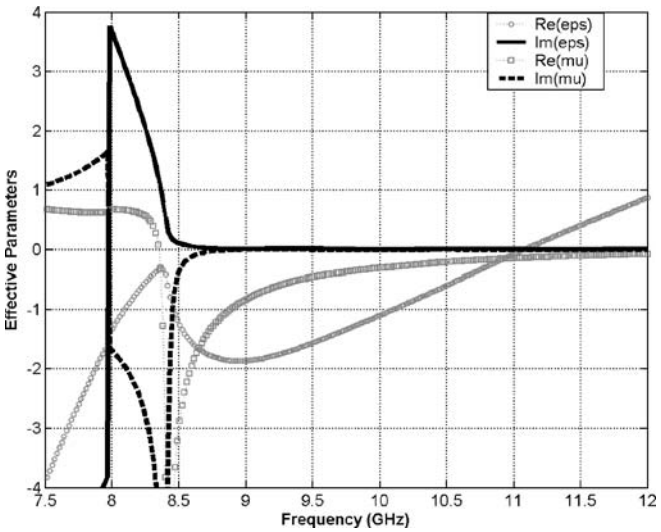

FIGURE 5 Illustration of the effective parameters of the DNG embedded in the substrate

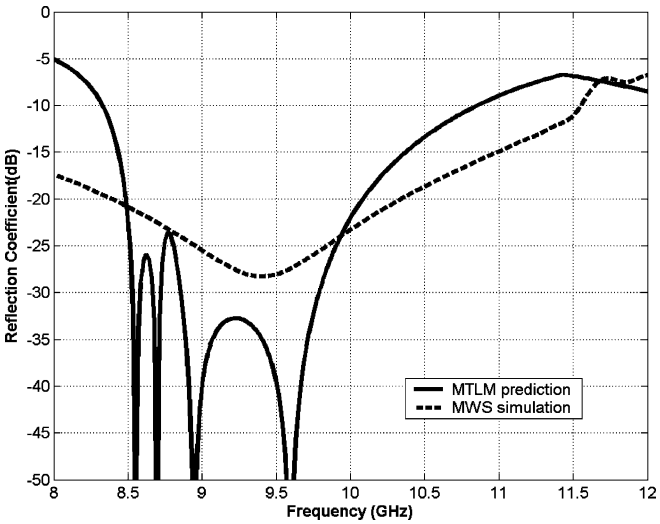

FIGURE 6 Illustration of the reflection coefficient obtained from MTLM prediction and CST MWS full-wave simulation

and performance. The feed of the antenna is assumed to match the antenna at 9 GHz. By embedded the effective parameters into the MTLM, the reflection coefficient got from MTLM prediction is illustrated in Fig. 6, represented by the solid line. The reflection coefficient abruptly drops to below -20 dB at 8.50 GHz and tardily goes back at about 10.08 GHz. Although the coefficient fluctuates in the band, it shows that the small MSA can radiate well with good input admittance. The relative bandwidth of -20 dB is about 17.56%. Additionally, the prediction suggests that the bandwidth of the MSA, partially loaded by DNG fillings, is mainly determined by the material resonant response and not by the antenna size, which is significantly different from traditional cases. To verify the predictions, the full-wave simulation is also conducted to the small MSA with DNG fillings by CST microwave studio (CST MWS). Under above situation, the reflection coefficient got from simulation is illustrated in Fig. 6 too, represented by the dash line. Based on the comparison and contrast, good agreement is demonstrated between the theoretical result and the full-wave simulation. Results also indicate that the coefficient at $10.40 \sim 11.05$ GHz is not as good as that at $8.50 \sim 10.08$ GHz, although the DNG fillings still support backward waves at $10.40 \sim 11.05$ GHz. One factor is that the backward wave wavelengths become larger when the operating frequency increases, which has been demonstrated in the first section.

4 Farfield pattern and *E*-field distribution of the small MSA

Besides the reflection coefficient, the farfield pattern is another important issue we concerned. The patterns, produced by both conventional half-wave-length MSAs and the small MSA with DNG fillings, are respectively demonstrated in Fig. 7. Figure 7a illustrates the bird's-eye view of the farfield pattern of the conventional half-wave-length patch working at 9 GHz loaded by normal dielectric medium with $\varepsilon_{\mathrm{r}} = 2.2$. In the pattern, the most intense distribution is along 0° direction, which is the main lobe, while

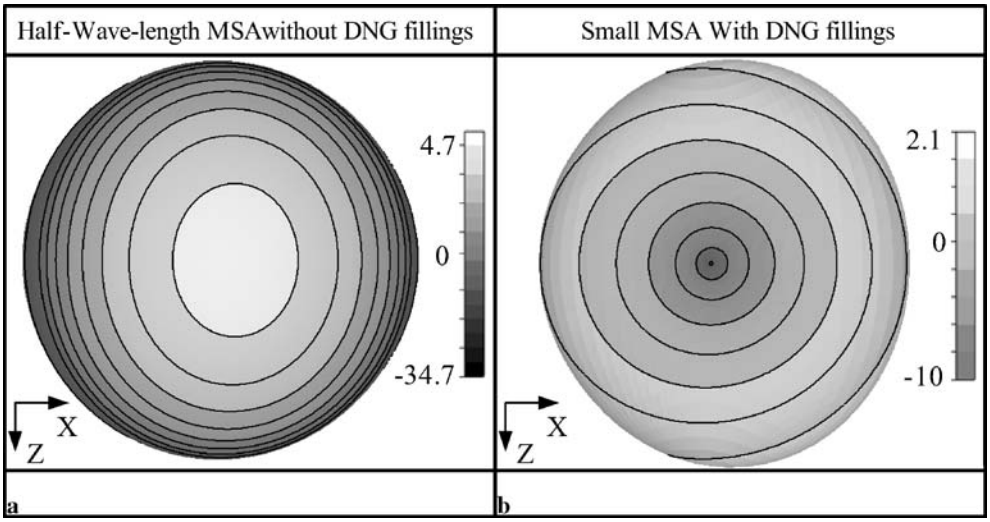

FIGURE 7 Comparison of the farfield patterns between the conventional half-wave-length MSA and the miniaturized MSA with DNG fillings (**a**) the pattern of the conventional MSA (**b**) the pattern of the small path with DNG fillings

it is very weak close to 90°. So the conventional MSA is a directive antenna with a main lobe perpendicular to the antenna patch. Figure 7b illustrates the bird's-eye view of the farfield pattern of the small MSA with DNG fillings at 9 GHz. In the pattern, the most intensive distributions are near 90°, while the pattern along 0° directions is very weak. Hence the small MSA with DNG fillings is omnidirectional.

To explain the truth of the difference of the farfield patterns, we had to look into the E-field distributions of the conventional MSAs and the small MSA with DNG fillings. Figure 8 illustrates the E-field distribution of the conventional half-wave-length MSA working at 9 GHz. It shows that the fringing fields distributed at the two edges are almost anti-phase in the substrate, because the patch is electrical half-wave-length, gaining 180°, when waves propagate along it. Furthermore, the E-field distribution located in the substrate determines that the farfield E-field is horizontal, just as the upper arrowhead annotated in Fig. 8. Figure 9 illustrates the E-field distribution of the small MSA with DNG fillings. It shows that the fringing fields distributed at the two edges are almost inphase in the substrate, which means the E-fields located at the two edges reach the wave crest or trough at the same time. Furthermore, the farfield E-field

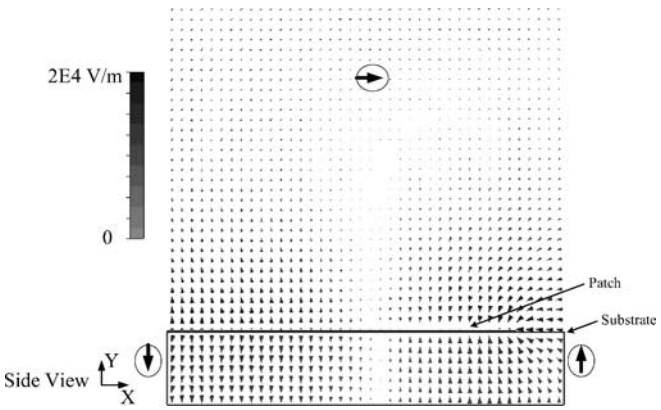

FIGURE 8 Illustration of the E-Field distribution of the conventional half-wave-length MSA without DNG fillings

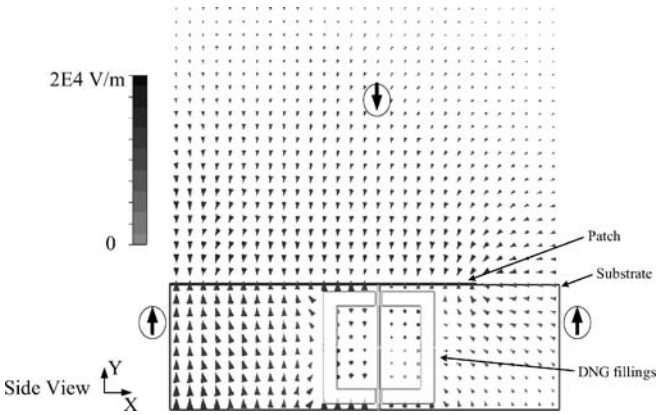

FIGURE 9 Illustration of the E-Field distribution of the small MSA with DNG fillings

is vertical as the upper arrowhead annotated in Fig. 9, determined by the E-field distribution located in the substrate. The difference is the root that leads to the definitely difference between the farfield patterns of small SMA and traditional ones.

5 Conclusion

In this investigation, DNG fillings are embedded in the substrate to composite a DPS-DNG-DPS substrate. Since they can support backward waves within $8.45 \sim 11.05$ GHz, the DNG fillings perform as a phase compensator to reduce the physical dimensions of the MSAs. According to the approach, a small MSA is modeled and verified by using the modified transmission line model (MTLM) and full-wave simulation. Results show that the length of the MSA has been significantly reduced to 0.17λ, and the bandwidth is enhanced to 17.56% compared to conventional half-wave-length MSAs. Furthermore, one of the most interesting results is that the farfield pattern is omnidirectional, considering conventional MSAs are directive. The unique performance is resulted from the in-phase fringing fields, distributed at the two radiative edges of the small MSA with DNG fillings, while they are always anti-phase in conventional half-wave-length MSAs.

ACKNOWLEDGEMENTS This work was supported by the Natural Science Foundation of China under Grant 60 571 026, and the foundation from National Key Laboratory of Electromagnetic Environment under Grant 514 860 303. In addition, the authors would like to appreciate CST Ltd. Germany, for providing important supports in using the CST MWS software.

REFERENCES

1 V.G. Veselago, Sov. Phys. Uspekhi **10**, 509 (1968)
2 D.R. Smith, Willie J. Padilla, D.C. Vier, S.C. Nemat-Nasser, S. Schultz, Phys. Rev. Lett. **84**, 4184 (2000)
3 R.A. Shelby, D.R. Smith, S. Schultz, Science **292**, 77 (2001)
4 A. Grbic, G.V. Eleftheriades, J. Appl. Phys. **92**, 5930 (2002)
5 T.J. Yen, W.J. Padilla, N. Fang, D.C. Vier, D.R. Smith, J.B. Pendry, D.N. Basov, X. Zhang, Science **303**, 1494 (2004)
6 G.V. Eleftheriades, A. K Iyer, P.C. Kremer, IEEE Trans. Microw. Theory Technol. **50**, 2702 (2002)
7 A. Sanada, C. Caloz, T. Itoh, IEEE Trans. Microw. Theory Technol. **52**, 1252 (2004)
8 D.R. Smith, J.B. Pendry, M.C.K. Wiltshire, Science **305**, 788 (2004)
9 M.F. Wu, F.Y. Meng, Q. Wu, J. Wu, Acta Phys. Sin. **55**, 5790 (2006)
10 M.F. Wu, Q. Wu, F.Y. Meng, J. Wu, Acta Phys. Sin. **55**, 6368 (2006)
11 L. Liu, C. Caloz, C.C. Chang, T. Itoh, J. Appl. Phys. **92**, 5560 (2002)
12 A. Erentok, P. Luljak, R.W. Ziolkowski, IEEE Trans. Antennas Propag. **53**, 160 (2005)
13 A. Alu, N. Engheta, IEEE Trans. Microw. Theory Technol. **52**, 199 (2004)
14 S.G. Mao, S.L. Chen, IEEE Trans. Antennas Propag. **54**, 1084 (2004)
15 S.G. Mao, S.L. Chen, C.W. Huang, IEEE Trans. Microw. Theory Technol. **53**, 1515 (2005)
16 N. Engheta, IEEE Antennas Wirel. Propag. Lett. **1**, 10 (2002)
17 Y. Li, L. Ran, H. Chen, J. Huangfu, X. Zhang, K. Chen, T.M. Grzegorczyk, J.A. Kong, IEEE Trans. Microw. Theory Technol. **53**, 1522 (2005)
18 S.F. Mahmoud, IEEE Antennas Wirel. Propag. Lett. **3**, 19 (2004)
19 W. Xu, L.W. Li, H.Y. Yao, T.S. Yeo, Q. Wu, J. Electromagn. Waves Appl. **19**, 2033 (2005)
20 S.A. Tretyakov, M. Ermutlu, IEEE Antennas Wirel. Propag. Lett. **4**, 266 (2005)
21 K. Buell, H. Mosallaei, K. Sarabandi, IEEE Trans. Microw. Theory Technol. **54**, 135 (2006)
22 Q. Wu, F.Y. Meng, H.L. Wang, J. Wu, L.W. Li, Key Note Paper In: 2006 International RF and Microwave Conference **1A**, 8 (2006)
23 L. Shen, S. He, S. Xiao, Phys. Rev. B **69**, 115 111 (2004)
24 R. Garg, P. Bhartia, I. Bahl, A. Ittipiboon, *Microstrip Antenna Design Handbook* (Artech House, Norwood, 2001), p. 164
25 R.W. Ziolkowski, IEEE Trans. Antennas Propag. **51**, 1516 (2003)